

Exploring the validity of the point source approximation

Thomas Eeken

May 14, 2014

Abstract

The point source approximation is widely used for earthquake representation because it is computationally efficient for certain kinds of synthetic calculations. It is based on the assumption that the seismic wave-field generated by a realistic source will match up with that generated by the corresponding centroid point source, as long as the waves investigated have sufficiently long wavelengths and periods. It is important to know whether this approximation is valid, otherwise unknown errors can be introduced into results based using the this approximation.

In order to get an idea of the validity of the point source approximation, we compare the wave-field generated by various distributions of point sources to that generated by the corresponding centroid point source. While the point source distributions used do not represent the full complexity of seismic sources, these tests are still useful to explore some of the effects of combining multiple point sources into a single centroid point source, which is what the point source approximation is based on.

In the case of an event consisting of two point sources, the time difference between the two point sources before the misfit with the centroid becomes significant, is approximately 7 seconds. In reality, this may represent events with durations over half the length of the shortest period investigated, since it is unlikely that all energy is released at the two ends of an event. For the spatial dimensions, the misfit may become significant for an offset close to 40 kilometres, while at 50 kilometres, around one third of the shortest wavelength, the misfit is already very large. Realistic rupture times indicate that for sources with spatial offset closer to 20 kilometres, the misfit should be very small. Events consisting of more than two point sources may interact in a way to create patches of high misfit that could affect stations located at the same location as these patches.

1 Introduction

Seismic sources are often complex internal deformations of the earth. Because it is infeasible to reconstruct the full complexity of the source region for modelling purposes, various ways of representing the seismic source have been used (see Madariaga (2007)). One commonly used representation is that of a point source. Backus and Mulcahy (1976) proposed the use of a point source moment tensor as a first order approximation of the source because this is efficient for certain kinds of synthetic calculations, especially those based on normal mode theory.

Any seismic source can be represented by a distribution of point sources (Dziewonski and Woodhouse, 1983). The accuracy of the representation will depend on the number of point sources, where a near infinite amount will be completely accurate. Of course, the number of point sources that can be inverted for is limited by our knowledge of the inside of the earth, the coverage of seismic data and the computational costs involved. For these reasons people often choose to invert for the centroid moment tensor of an event.

The centroid of a tensor field is defined as the point where the sum-of-squares of the first order moments is minimized (Backus, 1977). Such a centroid is a single point in space and time and can theoretically be calculated for any glut-rate distribution. Using a centroid moment tensor to represent a seismic event is only useful if the theoretical seismic energy radiation pattern of the centroid matches up with that of the actual source. It is generally stated that this will be the case for seismic waves with wavelengths that are sufficiently larger than the spatial dimensions of the source region and periods that are sufficiently longer than the duration of the event. We are, however, unaware of any systematic experiments to test this assumption.

One of the applications of the point source approximation is in the centroid-moment-tensor algorithm (Dziewonski et al., 1981; Dziewonski and Woodhouse, 1983). This algorithm is routinely applied to

seismic data by the global CMT (GCMT) project (see, for example, Ekström et al. (2012)). The centroid moment tensors from the GCMT catalogue are widely used across the geosciences. Many tomographic inversions make use of CMT parameters (for example, Panning and Romanowicz (2006); Ritsema et al. (2011)). The validity of the point source approximation is therefore quite important, otherwise unknown errors can be introduced into the resulting models.

In this paper we will look at the differences between the seismic wave-field generated by a source consisting of several point sources versus the same source, represented by the corresponding centroid moment tensor. First we do this by splitting a moment tensor up into two parts and placing them apart in time and/or space and generating synthetic seismograms for both the centroid and the split-up sources.

After this, we look at a distribution of moment tensors as inferred from InSAR data to obtain a more realistic example of a point source distribution and compare this with the corresponding centroid, again using synthetics.

We will also look at some of the effects of introducing source-time-functions to account for the fact that an event does not occur instantaneously at a single point in space.

2 Methods

2.1 Obtaining the centroid moment tensor

Stress and strain are generally accepted to be locally related through a linear law. However, during any event where rupture occurs along a fault, such a linear relation will not hold and there will be a difference between the stress predicted by the linear law and the actual stress. This difference is defined as the stress glut, Γ (Backus and Mulcahy, 1976). Any source will be characterized by a stress glut rate distribution, $\dot{\Gamma}(\mathbf{x}, t)$. The seismic moment tensor, \mathbf{M} is defined in terms of the stress glut rate, $\dot{\Gamma}$,

$$M_{ij} = \int_{t_1}^{t_2} \int_V \dot{\Gamma}_{ij}(\mathbf{x}', t') d^3x' dt' \quad (1)$$

where t_1, t_2 and V are the span of time and volume that contain all source processes associated with the event represented by the moment tensor. It is clear that the accuracy with which the point-source moment tensor represents the actual source depends on the size of the source region and how the stress glut changes over time throughout that region. The stress glut and moment tensor are related by integration, which is a linear operator. This means that if we split the stress glut into two parts,

$$\Gamma_{ij} = \Gamma_{ij}^{(1)} + \Gamma_{ij}^{(2)} \quad (2)$$

then that naturally results in the moment tensor being split into multiple corresponding parts as well,

$$M_{ij} = M_{ij}^{(1)} + M_{ij}^{(2)}. \quad (3)$$

The moment tensor representation will be close to completely accurate if the source is confined to a very small area as long as the glut-rate does not change too much throughout its duration. This means that if we split up the moment tensor into enough small parts, it will give a completely accurate representation of the source.

This also means that we can combine any distribution of point sources to obtain a centroid-moment-tensor, but clearly there is an extent for which this is a reasonable thing to do. Combining events days apart or located on opposite sides of the earth will not give an accurate representation.

Equation 3 gives us the zeroth-order moment tensor. In order to determine the centroid location and time for any source distribution, we need to make use of the first-order moments $\mathbf{\Lambda}$ and \mathbf{H} , which are defined

$$\Lambda_{ijk} = \int_{t_1}^{t_2} \int_V (x'_k - x_k) \dot{\Gamma}_{ij}(\mathbf{x}', t') d^3x' dt' \quad (4)$$

$$H_{ij} = \int_{t_1}^{t_2} \int_V (t' - t) \dot{\Gamma}_{ij}(\mathbf{x}', t') d^3x' dt'. \quad (5)$$

A similar linear relation between the stress glut and the first-order moments exist as for the zeroth-order moment. The centroid location in space and time, (\mathbf{x}_c, t_c) , are defined by minimising the sum-of-squares of the first-order moments, leading to the conditions

$$\frac{\partial}{\partial x_k} [\Lambda_{ijk}(\mathbf{x}) \Lambda_{ijk}(\mathbf{x})]_{\mathbf{x}=\mathbf{x}_c} = 0 \quad (6)$$

$$\therefore \Lambda_{ijk}(\mathbf{x}_c) \left[\frac{\partial \Lambda_{ijk}}{\partial x_k} \right]_{\mathbf{x}=\mathbf{x}_c} = 0 \quad (7)$$

and

$$\frac{\partial}{\partial t} [H_{ij}(t) H_{ij}(t)]_{t=t_c} = 0 \quad (8)$$

$$\therefore H_{ij}(t_c) \left[\frac{\partial H_{ij}}{\partial t} \right]_{t=t_c} = 0. \quad (9)$$

If we define our source to be acting at a single location with a given source time function $\tau(t - t_0)$ where the time of initial source activity is given by t_0 , then, following Dziewonski and Woodhouse (1983), we can write the stress glut as

$$\Gamma_{ij}(\mathbf{x}, t) = M_{ij} \delta^3(\mathbf{x} - \mathbf{x}_0) \tau(t - t_0). \quad (10)$$

Combining this with equation 1 we get

$$\begin{aligned} M_{ij} &= \int_{t_1}^{t_2} \int_V M_{ij} \delta^3(\mathbf{x} - \mathbf{x}_0) \dot{\tau}(t - t_0) d^3x' dt \\ &= M_{ij} [\tau(t_2 - t_0) - \tau(t_1 - t_0)]. \end{aligned} \quad (11)$$

We can use this and equation 9, keeping in mind that

$$\begin{aligned} \frac{\partial H_{ij}}{\partial t} &= - \int_{t_1}^{t_2} \int_V \dot{\Gamma}_{ij}(\mathbf{x}', t') d^3x' dt' \\ &= - M_{ij} \end{aligned} \quad (12)$$

to obtain

$$\begin{aligned} H_{ij}(t_c) M_{ij} &= M_{ij}^{(1)} \left(M_{ij}^{(1)} + M_{ij}^{(2)} \right) \left[\int_{t_1}^{t_2} t' \dot{\tau}(t' - t_0^{(1)}) dt' - t_c \int_{t_1}^{t_2} \dot{\tau}(t' - t_0^{(1)}) dt' \right] \\ &\quad + M_{ij}^{(2)} \left(M_{ij}^{(1)} + M_{ij}^{(2)} \right) \left[\int_{t_1}^{t_2} t' \dot{\tau}(t' - t_0^{(2)}) dt' - t_c \int_{t_1}^{t_2} \dot{\tau}(t' - t_0^{(2)}) dt' \right]. \end{aligned} \quad (13)$$

In general, all source time functions have the form

$$\tau(t) = \begin{cases} 0 & t < t_0 \\ \tau_0(t) & t_0 \leq t \leq t_{active} \\ 1 & t_{active} < t \end{cases} \quad (14)$$

Then, if $t_1 \leq t_0$ and $t_2 \geq t_0 + t_{active}$, we can write

$$\int_{t_1}^{t_2} \dot{\tau}(t - t_0^{(2)}) dt = 1 \quad (15)$$

and

$$\begin{aligned} \int_{t_1}^{t_2} t \dot{\tau}(t - t_0^{(2)}) dt &= \int_{t_0}^{t_0 + t_{active}} t \dot{\tau}(t - t_0^{(2)}) dt \\ &= t_0 + t_{active} - \int_{t_0}^{t_0 + t_{active}} \tau(t - t_0^{(2)}) dt \\ &= t_0 + t_{active} - T_I^{(2)}. \end{aligned} \quad (16)$$

If we then define $t_0^{(2)} = t_0^{(1)} + \delta t^{(2)}$, we can obtain the following expression for the centroid time:

$$t_c = \frac{1}{M_{ij}M_{ij}} [M_{ij}^{(1)}M_{ij}^{(1)}(t_0^{(1)} + t_{active}^{(1)} - T_I^{(1)}) + M_{ij}^{(1)}M_{ij}^{(2)}(t_0^{(1)} + t_{active}^{(1)} - T_I^{(1)}) \\ + M_{ij}^{(1)}M_{ij}^{(2)}(t_0^{(2)} + t_{active}^{(2)} - T_I^{(2)}) + M_{ij}^{(2)}M_{ij}^{(2)}(t_0^{(2)} + t_{active}^{(2)} - T_I^{(2)})] \quad (17)$$

$$t_c = t_0^{(1)} + \frac{\mathbf{M} : \mathbf{M}^{(1)}}{\mathbf{M} : \mathbf{M}} (t_{active}^{(1)} - T_I^{(1)}) \\ + \frac{\mathbf{M} : \mathbf{M}^{(2)}}{\mathbf{M} : \mathbf{M}} (\delta t^{(2)} + t_{active}^{(2)} - T_I^{(2)}) \quad (18)$$

where the superscripts are as in equation 3 and we make use of the double-dot product. Using similar methods for the location we get

$$\Lambda_{ijk}(\mathbf{x}_c)M_{ij} = (M_{ij}^{(1)} + M_{ij}^{(2)}) (\Lambda_{ijk}^{(1)}(\mathbf{x}) + \Lambda_{ijk}^{(2)}(\mathbf{x})) \\ = (M_{ij}^{(1)} + M_{ij}^{(2)}) \left\{ \left[(x_0^{(1)})_k - (x_c)_k \right] M_{ij}^{(1)} + \left[(x_0^{(2)})_k - (x_c)_k \right] M_{ij}^{(2)} \right\} = 0. \quad (19)$$

We can rearrange this and solve for the centroid location

$$M_{ij}M_{ij}(x_c)_k = M_{ij}M_{ij}^{(1)}(x_0^{(1)})_k + M_{ij}M_{ij}^{(2)}(x_0^{(2)})_k \\ = M_{ij}M_{ij}(x_0^{(1)})_k + M_{ij}M_{ij}^{(2)}(\delta x^{(2)})_k \\ (x_c)_k = (x_0^{(1)})_k + \frac{M_{ij}M_{ij}^{(2)}}{M_{ij}M_{ij}}(\delta x^{(2)})_k. \quad (20)$$

Here, we have defined the location of the second point source as $\mathbf{x}_0^{(2)} = \mathbf{x}_0^{(1)} + \delta \mathbf{x}^{(2)}$. Because we use a spherical reference frame, moment tensors moved around in space need to be rotated into their new reference frame. If, at position (θ, ϕ) , we have

$$\hat{\mathbf{e}}_{\mathbf{r}} = \sin \theta \cos \phi \hat{\mathbf{e}}_{\mathbf{x}} + \sin \theta \sin \phi \hat{\mathbf{e}}_{\mathbf{y}} + \cos \theta \hat{\mathbf{e}}_{\mathbf{z}} \quad (21)$$

$$\hat{\mathbf{e}}_{\theta} = \cos \theta \cos \phi \hat{\mathbf{e}}_{\mathbf{x}} + \cos \theta \sin \phi \hat{\mathbf{e}}_{\mathbf{y}} - \sin \theta \hat{\mathbf{e}}_{\mathbf{z}} \quad (22)$$

$$\hat{\mathbf{e}}_{\phi} = -\sin \phi \hat{\mathbf{e}}_{\mathbf{x}} + \cos \phi \hat{\mathbf{e}}_{\mathbf{y}} \quad (23)$$

then at a new position $(\theta + \delta\theta, \phi + \delta\phi)$, we will have

$$\hat{\mathbf{e}}'_{\mathbf{r}} = \sin(\theta + \delta\theta) \cos(\phi + \delta\phi) \hat{\mathbf{e}}_{\mathbf{x}} + \sin(\theta + \delta\theta) \sin(\phi + \delta\phi) \hat{\mathbf{e}}_{\mathbf{y}} + \cos(\theta + \delta\theta) \hat{\mathbf{e}}_{\mathbf{z}} \quad (24)$$

$$\hat{\mathbf{e}}'_{\theta} = \cos(\theta + \delta\theta) \cos(\phi + \delta\phi) \hat{\mathbf{e}}_{\mathbf{x}} + \cos(\theta + \delta\theta) \sin(\phi + \delta\phi) \hat{\mathbf{e}}_{\mathbf{y}} - \sin(\theta + \delta\theta) \hat{\mathbf{e}}_{\mathbf{z}} \quad (25)$$

$$\hat{\mathbf{e}}'_{\phi} = -\sin(\phi + \delta\phi) \hat{\mathbf{e}}_{\mathbf{x}} + \cos(\phi + \delta\phi) \hat{\mathbf{e}}_{\mathbf{y}} \quad (26)$$

Any position vector, \mathbf{v} , can be written in terms of both systems,

$$\mathbf{v} = v_r \hat{\mathbf{e}}_{\mathbf{r}} + v_{\theta} \hat{\mathbf{e}}_{\theta} + v_{\phi} \hat{\mathbf{e}}_{\phi} \quad (27)$$

$$= v'_r \hat{\mathbf{e}}'_{\mathbf{r}} + v'_{\theta} \hat{\mathbf{e}}'_{\theta} + v'_{\phi} \hat{\mathbf{e}}'_{\phi} \quad (28)$$

Therefore we have

$$\begin{pmatrix} \sin \theta \cos \phi & \cos \theta \cos \phi & -\sin \phi \\ \sin \theta \sin \phi & \cos \theta \sin \phi & -\sin \phi \\ \cos \theta & -\sin \theta & 0 \end{pmatrix} \begin{pmatrix} v_r \\ v_{\theta} \\ v_{\phi} \end{pmatrix} \\ = \begin{pmatrix} \sin(\theta + \delta\theta) \cos(\phi + \delta\phi) & \cos(\theta + \delta\theta) \cos(\phi + \delta\phi) & -\sin(\phi + \delta\phi) \\ \sin(\theta + \delta\theta) \sin(\phi + \delta\phi) & \cos(\theta + \delta\theta) \sin(\phi + \delta\phi) & -\sin(\phi + \delta\phi) \\ \cos(\theta + \delta\theta) & -\sin(\theta + \delta\theta) & 0 \end{pmatrix} \begin{pmatrix} v'_r \\ v'_{\theta} \\ v'_{\phi} \end{pmatrix} \quad (29)$$

which can be written as

$$\mathbf{R}(\theta, \phi) \begin{pmatrix} v_r \\ v_\theta \\ v_\phi \end{pmatrix} = \mathbf{R}(\theta + \delta\theta, \phi + \delta\phi) \begin{pmatrix} v'_r \\ v'_\theta \\ v'_\phi \end{pmatrix} \quad (30)$$

and from this we can obtain an expression for a position vector in the new reference frame

$$\begin{pmatrix} v'_r \\ v'_\theta \\ v'_\phi \end{pmatrix} = \mathbf{R}^{-1}(\theta + \delta\theta, \phi + \delta\phi) \mathbf{R}(\theta, \phi) \begin{pmatrix} v_r \\ v_\theta \\ v_\phi \end{pmatrix}. \quad (31)$$

2.2 Calculation of synthetic seismograms

In order to investigate the difference between distributions of moment tensors and the corresponding centroid moment tensor, we use synthetic seismograms. These synthetics are generated using a fully numerical wave propagation code (SPECFEM3D_GLOBE v.5.1.1, Komatitsch and Tromp (2002a,b); Komatitsch et al. (2010)) with the degree-20 earth model S20RTS (Ritsema et al., 1999), which is built on PREM, and the crust2.0 model (Bassin et al., 2000). Seismograms are recorded at a global distribution of stations including station locations based on the IRIS/IDA and IRIS/USGS networks (network codes II and IU) as well as a more even distribution of theoretical station locations to see how differences vary across the globe. The code is run separately for individual point sources. In order to create the wave-field for the point-source distributions, the synthetics of the individual point-sources are added together. The computed synthetics are all 100 minutes long and are accurate to periods of approximately 20 seconds.

Several time-frequency windows are obtained from each trace because different parts of the seismogram are sensitive to different kinds of data. The first part of the seismogram generally contains the body waves, which travel through the earth while surface waves are mostly sensitive to the crust and upper mantle. These windows are as described in table 1 and are chosen to match up with the range of frequencies used in the algorithm for the global CMT project (Ekström et al., 2012). The first window, BODY, is intended to cover the body waves while the second window, SURF, covers the intermediate-period surface waves.

name	window		filter			
	start	end	T_1	T_2	T_3	T_4
BODY	P-300s	R1-300s	150	125	60	50
SURF	R1-300s	R2+600s	150	125	60	50

Table 1: Definitions of the time-frequency windows used in this study. P is the time of the first arrival of the P, p, Pdiff, PKP or PKIKP phase as calculated for PREM. R1 and R2 represent the arrivals of the first and second Rayleigh waves for a surface wave speed of 4 km/s. T_1, \dots, T_4 represent the four corner frequencies of the cosine bandpass filter.

2.3 Misfit calculation

To assess how well the waveforms generated by a source defined by the centroid moment tensor matches up with those generated by the distribution of sources, we will look at the misfit between the seismograms computed for both cases. For clarity, we will use the term data from now on to describe the waveforms generated for the distributed moment tensors and synthetics to describe those generated by the centroid moment tensor. We make use of the least-squares waveform misfit

$$m^2(\mathbf{d}, \mathbf{s}) = \frac{(\mathbf{d} - \mathbf{s})^T (\mathbf{d} - \mathbf{s})}{\mathbf{d}^T \mathbf{d}} \quad (32)$$

This would give a value for m^2 of 0 if the two datasets match up perfectly, while a value greater than 1 would mean that the difference is larger than the data.

3 Results

In this section we will investigate how similar the seismic wave-field generated by a source represented by multiple point source moment tensors is to that of one represented by the corresponding centroid moment tensor. For comparison, we shall first look at the global difference between a single point source event at a depth of 12 kilometres versus a single point source with the same moment tensor but located at a depth of 62 kilometres. The source parameters used in our experiments are given in table 2.

Valentine and Trampert (2012) have investigated the uncertainties in the seismic source parameters of an event, as determined by the CMT algorithm. Depending on the level of misfit that is considered acceptable, they find that the uncertainty in the depth determination is closer to 20 kilometres than 50 kilometres. Therefore you would expect to find significant differences between the two data sets, which is reflected in the misfit.

The difference in the body-wave window (figure 1) is most apparent in the vertical component of the seismograms, especially the striking circular pattern surrounding the event site. Differences in the other two components are relatively small for the most part, although not negligible, and there are some patches of greater misfit closer to the sources.

The misfit pattern for the intermediate period surface waves (figure 2) is significantly different, showing both areas with larger misfit as well as large areas where the misfit approaches zero. The vertical component appears to be split up into four parts. The lines separating the quadrants appear to line up with the nodal planes from the source mechanisms. The North component also appears to be divided into quadrants, but rotated 45 degrees. The misfit in the East component appears to make a cross shape with an angle of 45 degrees with the nodal planes.

Clearly, the wave-fields generated by two sources at such different depths are not the same. This is as you would expect, since sources at different depths will excite different modes of oscillation, affecting different parts of the seismograms. If the differences between a moment tensor distribution and the corresponding centroid are of a similar size, then the point source approximation would clearly not be valid for that source.

3.1 Splitting the source in time

At first we take the source located at a depth of 12 kilometres and simply split it into two parts of equal size, located at the same location. We can now set the two halves apart in time. Of course there is a limit to the offset in time for which a single centroid will be accurate. Figures 3 and 4 show how the least squares misfit of the vertical component varies with the difference offset for several stations at different points on the earth's surface. Clearly the difference remains very small if the time between sources is not too large. If the two events occur within 7 seconds of each other, the difference with the point source is pretty much insignificant. After that point, the difference starts to increase to a point where the misfit is comparable to what would be expected from noise in the data, at around 15 seconds. At 30 seconds of offset, the misfit is already several times larger than the data. This means that such an event, consisting of two pulses at more than 15 seconds apart, will not be accurately represented by a single point source.

Splitting the same source at a depth of 62 kilometres gives similar results (figures 5 and 6) but the increase in misfit occurs at slightly larger offsets, indicating that depth may play a role in how far apart sources can be placed in time before the wave-field starts to differ significantly from that of the centroid. This may be the result of the fact that earthquakes at different depths will excite different modes, and thus different frequencies, affecting different parts of the seismogram. Therefore depth will influence the range of moment tensor distributions that agree with the same centroid.

3.2 Source time functions

So far we have assumed that every moment tensor represents an instantaneous event which, of course, is not a correct assumption. In order to incorporate a more realistic time dependency of the release of seismic energy, a source time function can be used. At first we convolve the seismograms of each source from the previous section with a triangular source time function (fig. 11a) with a half-width of 7.5 seconds. This half-width is the same as would be used in the inversion process of the global CMT project for an earthquake with an equivalent seismic moment to that of the centroid used in the previous section (Ekström et al., 2012).

moment tensor	f_1	f_2	f_3	f_4	f_5	f_6	ϕ_c	θ_c	z_c
Darfield									
<i>centroid</i>	6.398×10^{25}	-2.220×10^{25}	-4.178×10^{25}	7.663×10^{25}	-1.698×10^{25}	-3.572×10^{26}	172.1962	-43.5863	5.16
<i>segment1</i>	-1.013×10^{25}	-4.726×10^{25}	5.739×10^{25}	2.384×10^{25}	8.207×10^{23}	-2.444×10^{25}	171.9982	-43.5483	4.7
<i>segment2</i>	1.831×10^{24}	-1.831×10^{24}	-1.530×10^{10}	1.303×10^{25}	-8.734×10^{24}	-1.249×10^{26}	172.1401	-43.5979	4.7
<i>segment3</i>	8.652×10^{23}	4.329×10^{25}	-4.416×10^{25}	1.275×10^{25}	2.273×10^{23}	-7.660×10^{25}	172.2515	-43.5873	4.5
<i>segment4</i>	1.567×10^{25}	-1.567×10^{25}	-9.819×10^{09}	2.948×10^{25}	-1.999×10^{25}	-8.018×10^{25}	172.3253	-43.5941	7.2
<i>segment5</i>	-6.034×10^{24}	6.034×10^{24}	-2.316×10^{09}	-4.714×10^{24}	-9.222×10^{24}	-1.891×10^{25}	172.4064	-43.5961	4.3
<i>segment6</i>	2.757×10^{23}	7.779×10^{24}	-8.054×10^{24}	-2.698×10^{24}	-5.819×10^{23}	-7.453×10^{24}	172.2153	-43.5553	3.0
<i>segment7</i>	3.944×10^{25}	-5.065×10^{24}	-3.437×10^{25}	7.515×10^{24}	1.958×10^{25}	-1.320×10^{25}	172.1582	-43.5809	4.8
<i>segment8</i>	2.225×10^{25}	-1.140×10^{25}	-1.085×10^{25}	-1.640×10^{24}	7.458×10^{23}	-1.125×10^{25}	171.9081	-43.5602	3.4
12km depth									
<i>centroid</i>	3.825×10^{25}	8.191×10^{23}	-3.911×10^{25}	4.920×10^{25}	1.568×10^{24}	-3.600×10^{26}	171.8100	-43.5600	12.0
0km apart									
<i>segment</i>	1.913×10^{25}	4.096×10^{23}	-1.956×10^{25}	2.460×10^{25}	7.84×10^{23}	-1.800×10^{26}	171.8100	-43.5600	12.0
10km apart									
<i>segment1</i>	1.920×10^{25}	3.765×10^{23}	-1.960×10^{25}	2.455×10^{25}	5.025×10^{23}	-1.800×10^{26}	172.1250	-43.6045	12.0
<i>segment2</i>	1.920×10^{25}	3.765×10^{23}	-1.960×10^{25}	2.455×10^{25}	5.025×10^{23}	-1.800×10^{26}	172.1150	-43.5155	12.0
20 km apart									
<i>segment1</i>	1.904×10^{25}	4.432×10^{23}	-1.951×10^{25}	2.465×10^{25}	1.068×10^{24}	-1.800×10^{26}	172.1099	-43.4702	11.99
<i>segment2</i>	1.920×10^{25}	3.763×10^{23}	-1.960×10^{25}	2.455×10^{25}	4.999×10^{23}	-1.800×10^{26}	172.1301	-43.6598	11.99
50 km apart									
<i>segment1</i>	1.893×10^{25}	4.943×10^{23}	-1.945×10^{25}	2.473×10^{25}	1.494×10^{24}	-1.800×10^{26}	172.0949	-43.3355	11.95
<i>segment2</i>	1.932×10^{25}	3.271×10^{23}	-1.967×10^{25}	2.447×10^{25}	7.380×10^{22}	-1.800×10^{26}	172.1453	-43.7845	11.95
62km depth									
<i>centroid</i>	3.825×10^{25}	8.191×10^{23}	-3.911×10^{25}	4.920×10^{25}	1.568×10^{24}	-3.600×10^{26}	171.8100	-43.5600	62.0
0km apart									
<i>segment</i>	1.913×10^{25}	4.096×10^{23}	-1.956×10^{25}	2.460×10^{25}	7.84×10^{23}	-1.800×10^{26}	171.8100	-43.5600	62.0

Table 2: The parameters used for the different moment tensors. f_1, \dots, f_6 are the six components of the moment tensor. ϕ_c and θ_c are the latitude and longitude respectively and z_c is the depth of the source.

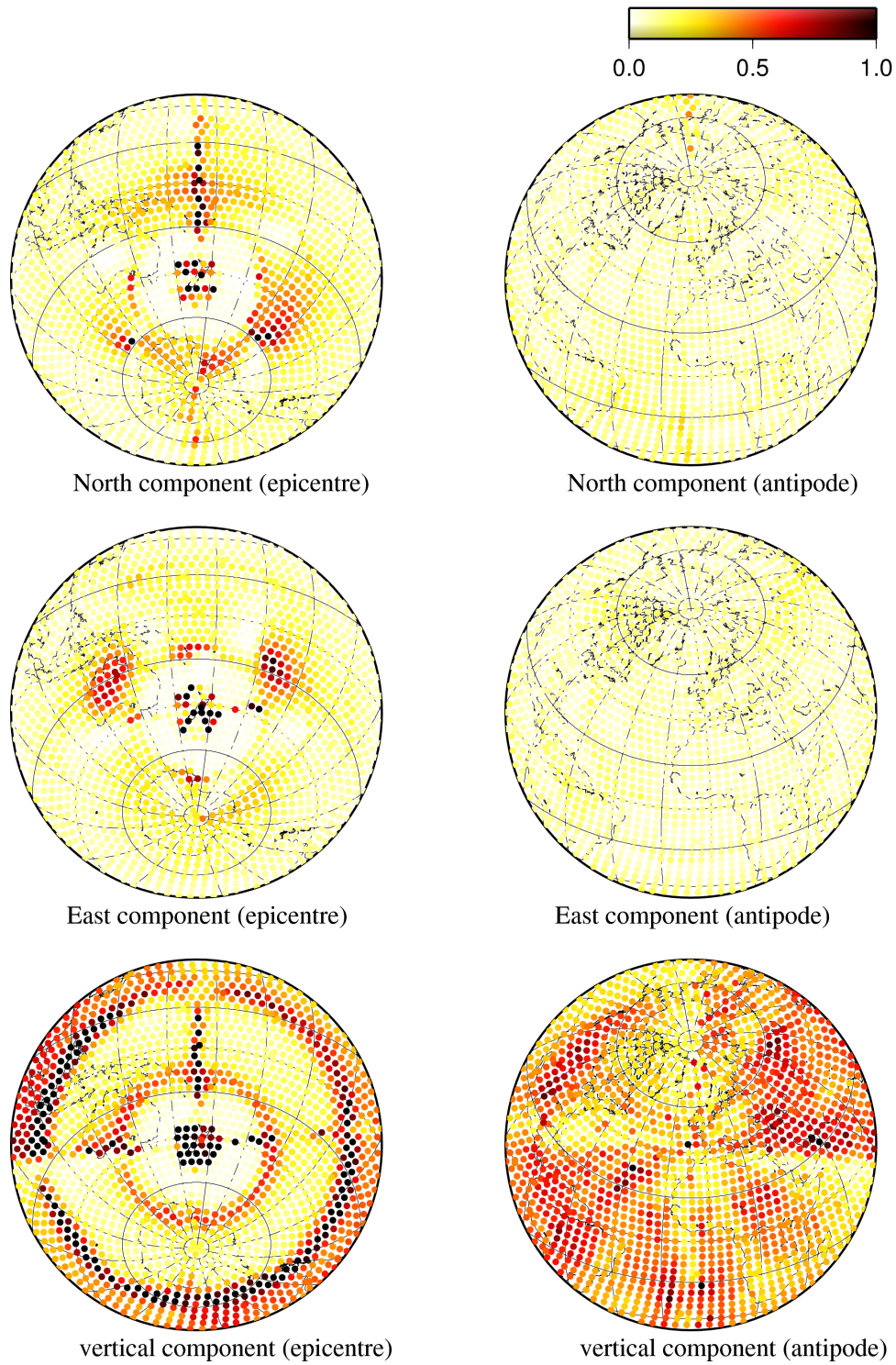


Figure 1: The waveform misfit between the wave-field generated by two sources represented by the same moment tensor, one located at a depth of 12 kilometres and one at a depth of 62 kilometres. The data has been filtered to the BODY time-frequency window as described in table 1. The misfit for the North and East components is not very large, but surrounding the epicentre there is a small cluster where the misfit is very large, followed by a circle of minimum misfit. Outside this circle the misfit is more or less the same across the globe, except for some patches just outside the circle where the misfit is noticeably higher. The vertical component has a circular pattern surrounding the epicentre of higher and lower misfits. The globe also appears to be split into quadrants.

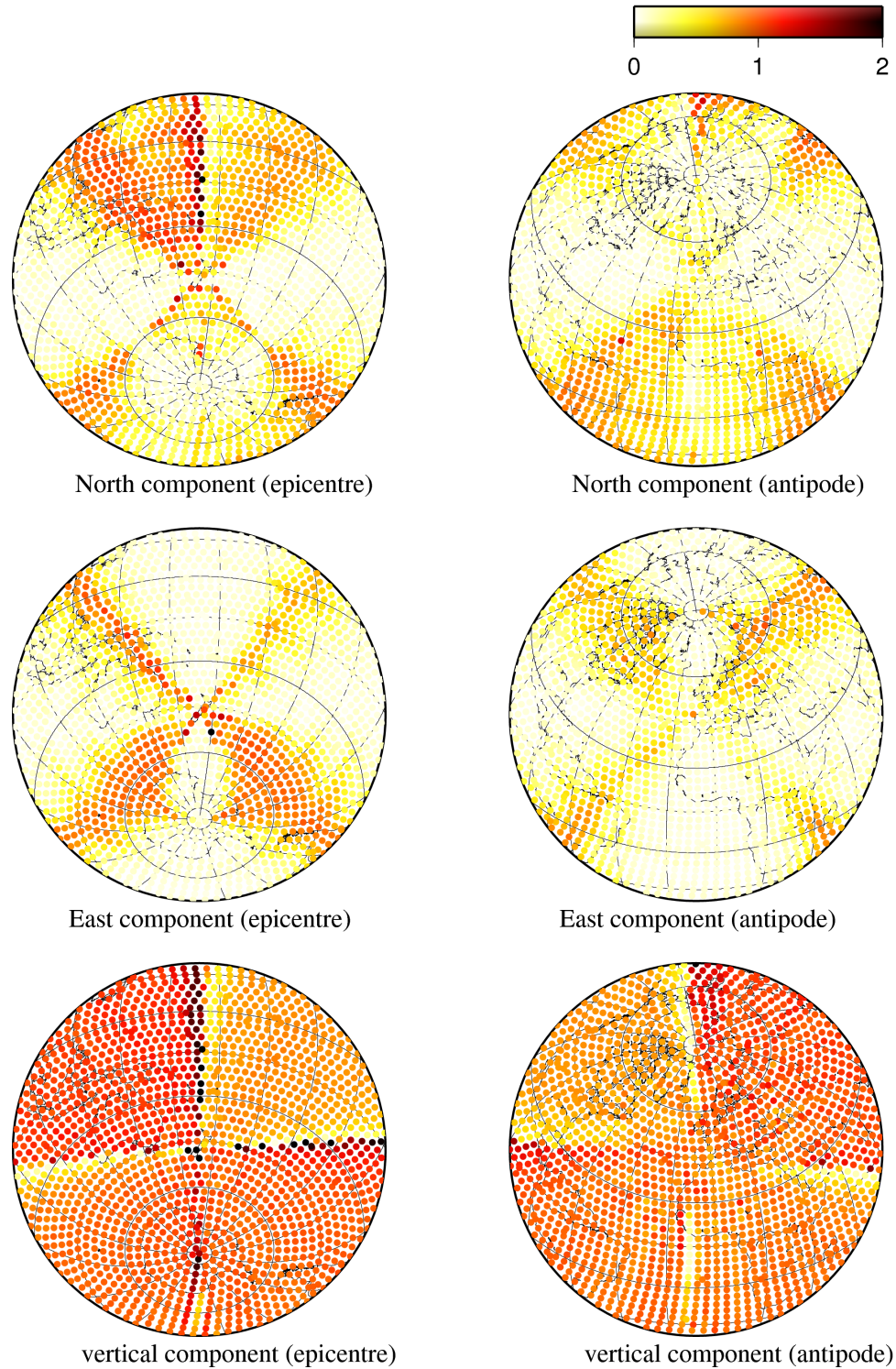


Figure 2: The waveform misfit between the wave-field generated by two sources represented by the same moment tensor, one located at a depth of 12 kilometres and one at a depth of 62 kilometres. The data has been filtered to the SURF time-frequency window as described in table 1. All three components appear to split the globe into quadrants, although there is a difference in orientation between the horizontal and vertical components.

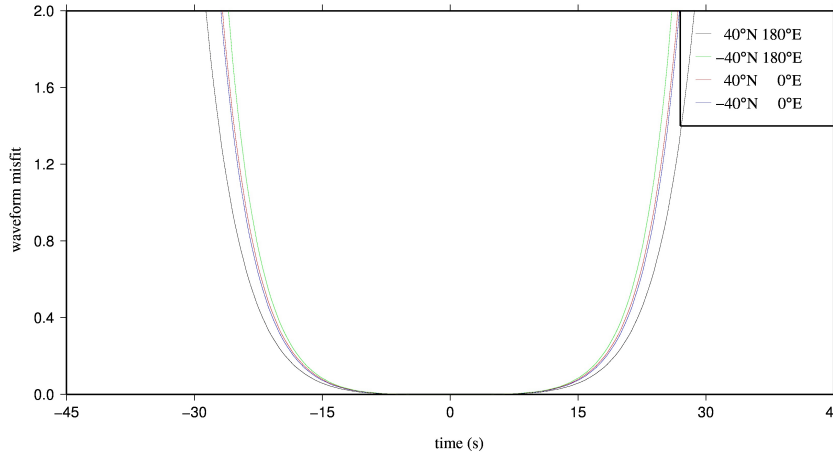


Figure 3: The waveform misfit with the centroid for two sources of equal size, located at the same location at 12 km depth, as a function of the temporal offset between them. This data is from the vertical component of 4 stations across the globe, one station at -40 degrees North and 180 degrees East, very close to the source. One station at the exact opposite end of the first stations at 40 degrees North and 0 degrees East and 2 stations halfway on the arc paths connecting the two stations at -40 degrees North and 0 degrees East and at 40 degrees North and 180 degrees East. The data has been filtered to the BODY window.

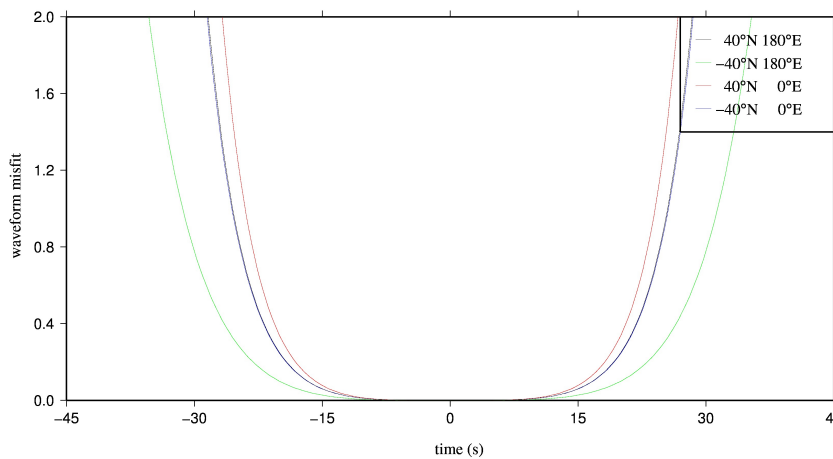


Figure 4: The waveform misfit with the centroid for two sources of equal size, located at the same location at 12 km depth, as a function of the temporal offset between them. This data is for the vertical component and has been filtered to the SURF window.

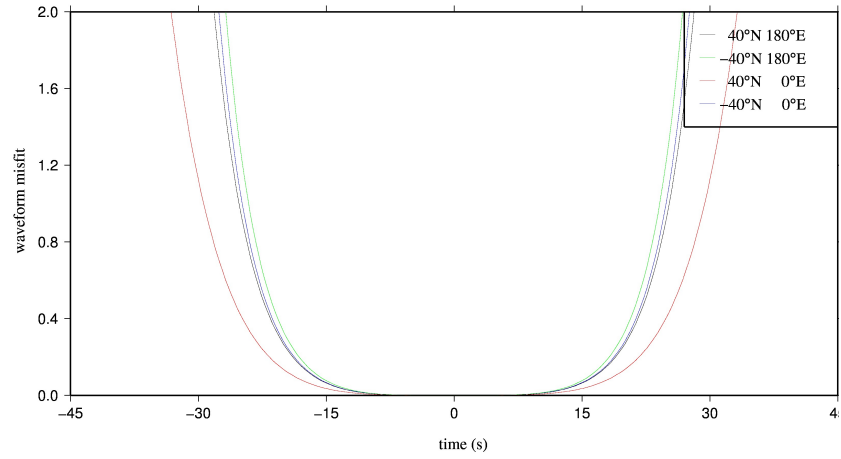


Figure 5: The waveform misfit with the centroid for two sources of equal size, located at the same location at 62 km depth, as a function of the temporal offset between them. This data is from the vertical component and has been filtered to the BODY window.

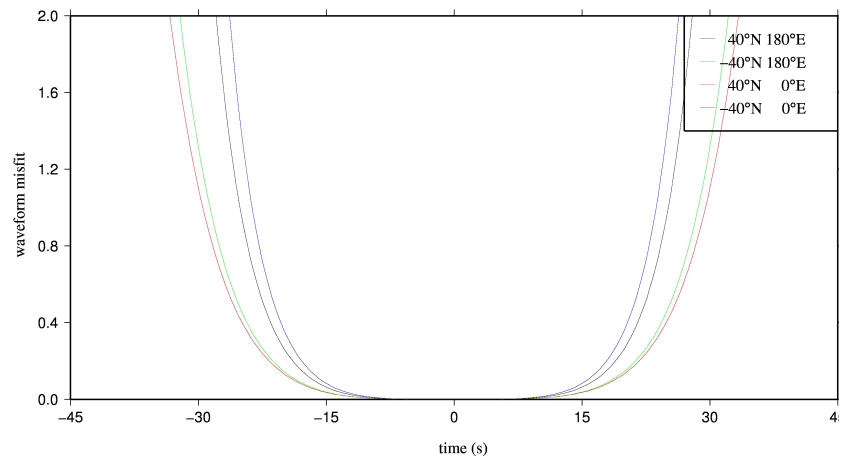


Figure 6: The waveform misfit with the centroid for two sources of equal size, located at the same location at 62 km depth, as a function of the temporal offset between them. This data is for the vertical component and has been filtered to the SURF window.

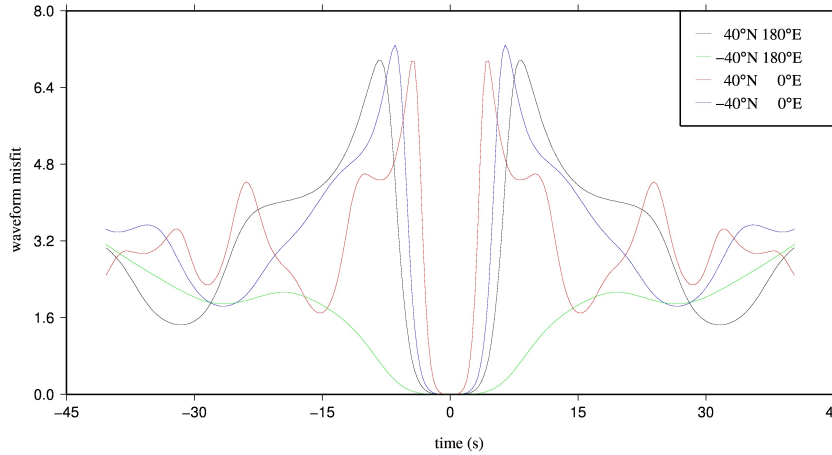


Figure 7: The waveform misfit with the centroid for two sources of equal size, located at the same location at 12 km depth, as a function of the temporal offset between them. This is unfiltered data of the North components of the four stations.

Figures 7 and 8 show the effect of the introduction of a source time function on unfiltered data, clearly decreasing the maximum misfit. It also has more complex effects on the size of the misfit as a result of offset time. First of all, it broadens the range of time offsets for which all stations show a misfit smaller than 1. Furthermore, it smoothes out a lot of the peaks and troughs in the misfit curve, although the different stations still show different peaks and troughs that seem to be a function of the distance from the source. These peaks and troughs will be the result of the way higher frequencies generated by the different smaller point sources are summed, generating comparatively large or small amplitudes in the data and affecting the misfit as a result.

When comparing filtered data convolved with a source time function (figures 9 and 10) with filtered data without (figures 5 and 6), the differences are comparatively small, although there is a very slight decrease in misfit. The fact that the addition of these source-time functions hardly affects the misfit means that the point source approximation appears to be valid for a combined duration of the source time functions of up to 22 seconds. For events up to 30 seconds, the misfit is still only comparable to what would be expected of noise. These durations are around half the length of the shortest periods investigated. However, the misfit appears to be governed mostly by the distance between the peaks, longer durations due to greater half-widths of the source-time function do not appear to have very significant effects on the misfit.

Using the same source time function for both the smaller sources and the centroid is naturally inaccurate if there is any time offset. A more accurate source time function for the centroid would match the superposition of the two triangles of the individual source time functions, like depicted in figure 11b and c. If we implement this, we get a misfit dependence on time offset like in figures 12 and 13. The misfit at larger offset has been decreased dramatically compared to the use of a more simple triangular source time function, but the misfit starts to increase for smaller offsets. This difference is still very small compared to the size of the data. The reason for this increase in misfit is quite unclear. Since the sources are located at the same location, this should provide an exact solution, but that is clearly not the case.

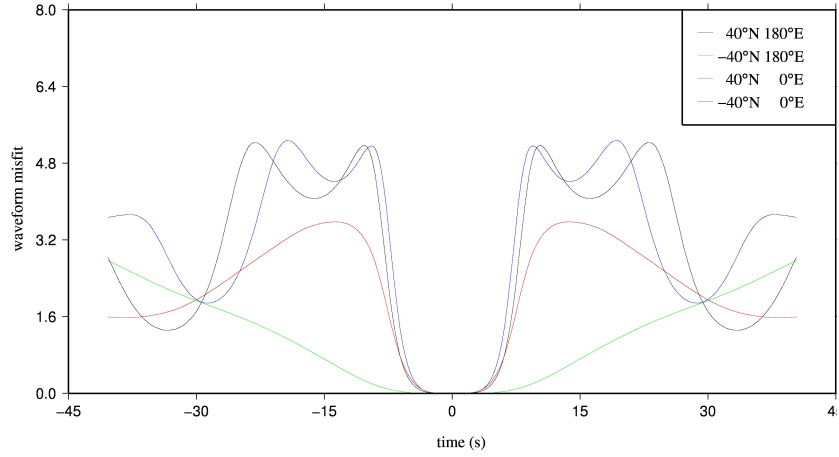


Figure 8: The waveform misfit with the centroid for two sources of equal size, located at the same location at 12 km depth, as a function of the temporal offset between them. This is unfiltered data from the North components, convolved with a triangular source-time function with a half-width of 7.5 seconds.

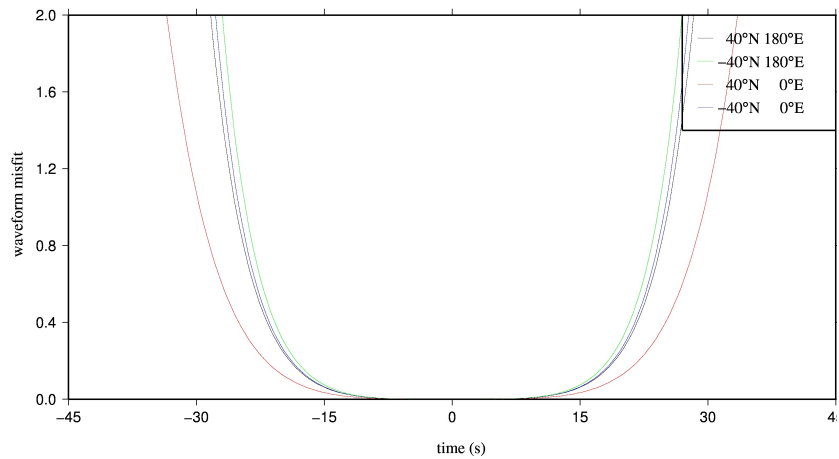


Figure 9: The waveform misfit with the centroid for two sources of equal size, located at the same location at 62 km depth, as a function of the temporal offset between them. This is data from the vertical components, filtered to the BODY window and convolved with a triangular source-time function with a half-width of 7.5 seconds.

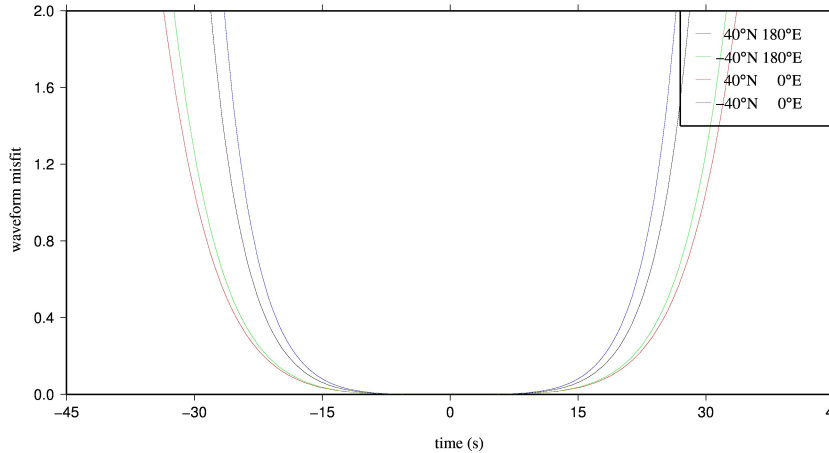


Figure 10: The waveform misfit with the centroid for two sources of equal size, located at the same location at 62 km depth, as a function of the temporal offset between them. This is data from the vertical components, filtered to the SURF window and convolved with a triangular source-time function with a half-width of 7.5 seconds.

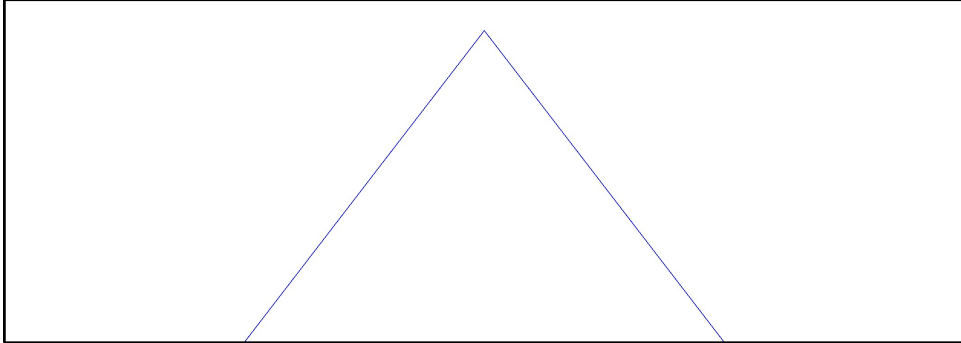
3.3 Splitting the source in space

In reality, seismic sources are generally distributed in space as well as time. Splitting the source at 12 kilometres depth into two equal parts and placing them apart in space rather than time, we can get some idea of how a spatial distribution affects the misfit. Placing the parts approximately 10 or 20 km apart along one of the nodal planes, the misfit for most stations across the globe is considerably smaller than 0.01 in all components for filtered data, indicating that the centroid gives a very good representation of these source distributions. Apparently splitting the source over these distances has very little effect on the misfit within the time-frequency windows investigated.

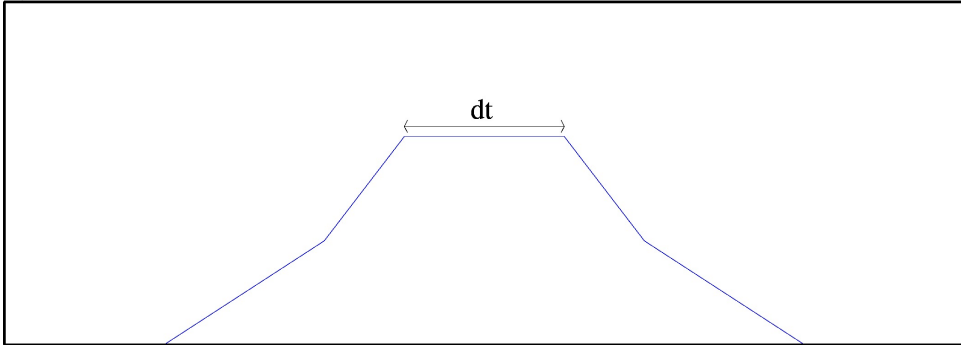
When placing the sources 50 km apart, however, the misfit approaches the size of the data as shown in figures 14 and 15. At this point the centroid is clearly no longer a good representation of the source distribution. The misfit appears to vary around 0.7, with some clusters of stations with considerably smaller or larger misfits. Within the vertical components, there is some hint of patterns. The body waves in figure 14 show two rings of slightly smaller misfit around the epicentre, while the surface waves have two lines of slightly larger misfit crossing near the epicentre, splitting this side of the globe in four quadrants, lining up with the nodal planes of the centroid.

It is difficult to relate this offset in space between sources to the magnitude of an event, since the seismic moment of an earthquake event is not only dependent on the fault area, but also on the amount of slip along the fault plane and the material properties of the rock that is rupturing. An event can consist of one or more segments. In case of the latter, an event of the same amount of fault surface and slip along that surface can be spread out over a larger (or smaller) area than would be the case for a single fault. For example, Elliot et al. (2012) have reconstructed an event of moment magnitude 7.1 to consist of 8 segments with magnitudes ranging from 6.0 to 6.7, where the largest segment has a length of 12 km and a width of 9.4 km, while another segment of magnitude 6.5 has a length of 14.7 km and a width of 9.3 km. If all the segments would lie end to end then the total length would be close to 63 kilometres, but the area encompassing the centroids of all the individual segment is approximately 38 by 4 km. Clearly the case of two point sources, 50 kilometres apart is not necessarily an extreme in comparison, given a magnitude of the centroid of 7.0.

a) $dt = 0s$



b) $dt = 2/3 \times hdur$



c) $dt = 4/3 \times hdur$

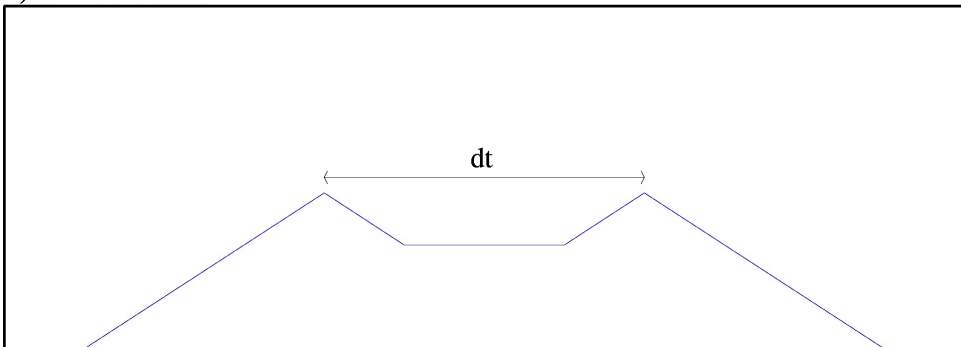


Figure 11: Three different source time functions consisting of two triangles set apart a) 0, b) $\frac{1}{3}$ or c) $\frac{4}{3}$ times the half-width of the individual triangles.

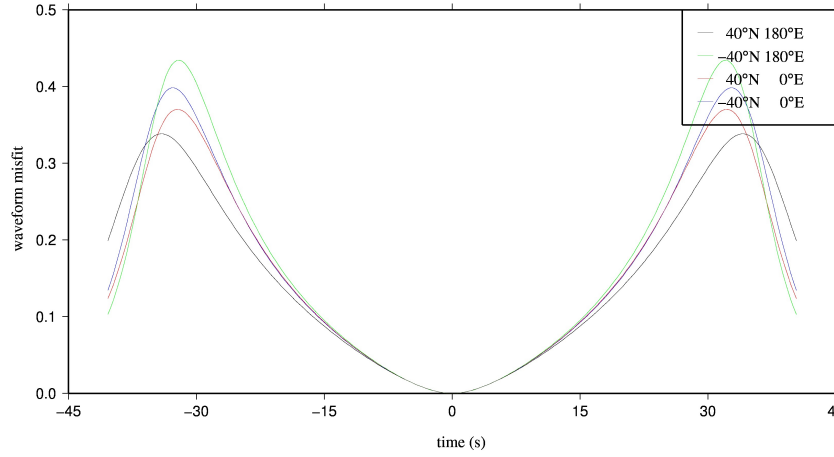


Figure 12: The waveform misfit with the centroid for two sources of equal size, located at the same location at 12 km depth, as a function of the temporal offset between them. This is data from the vertical component and has been filtered to the BODY window. The smaller sources are each convolved with a triangular source-time function with a half-width of 7.5 seconds and the centroid is convolved with a source-time function consisting of the sum of two triangles offset in time to match up with those of the smaller sources.

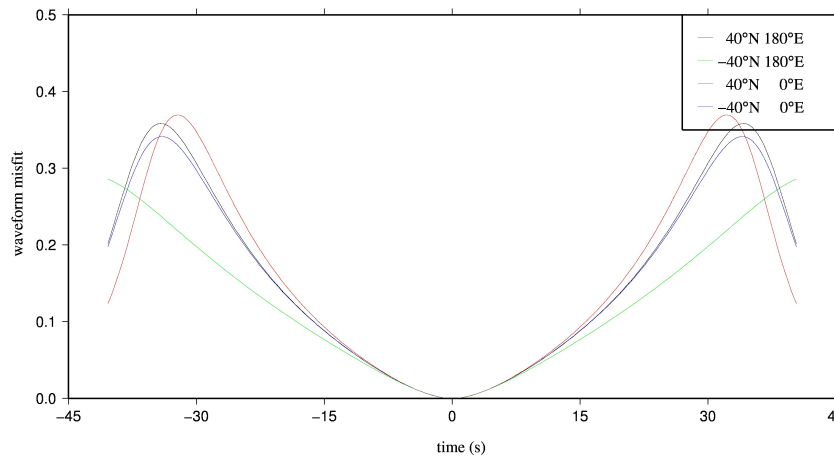


Figure 13: The waveform misfit with the centroid for two sources of equal size, located at the same location at 12 km depth, as a function of the temporal offset between them. This is data from the vertical component and has been filtered to the SURF window. The smaller sources are each convolved with a triangular source-time function with a half-width of 7.5 seconds and the centroid is convolved with a source-time function consisting of the sum of two triangles offset in time to match up with those of the smaller sources.

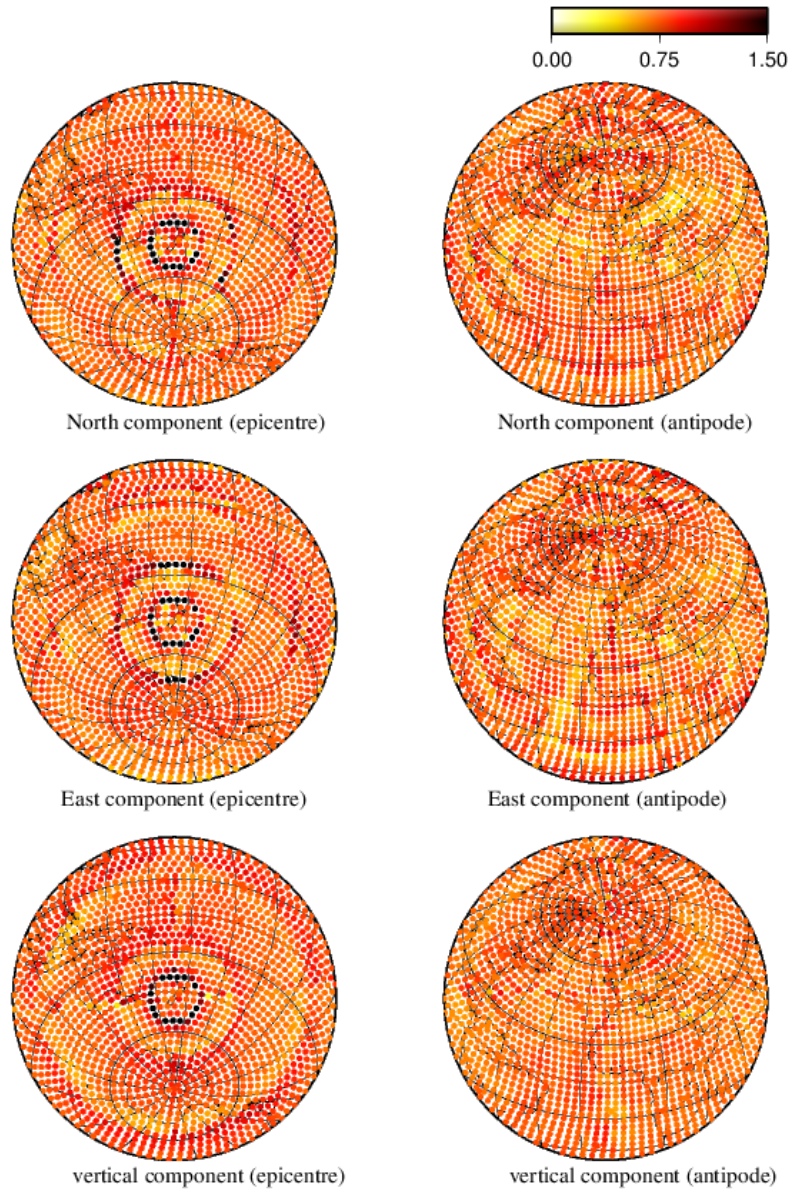


Figure 14: The waveform misfit between the centroid and two smaller sources of equal size, placed 50km apart. This data has been filtered to the BODY window.

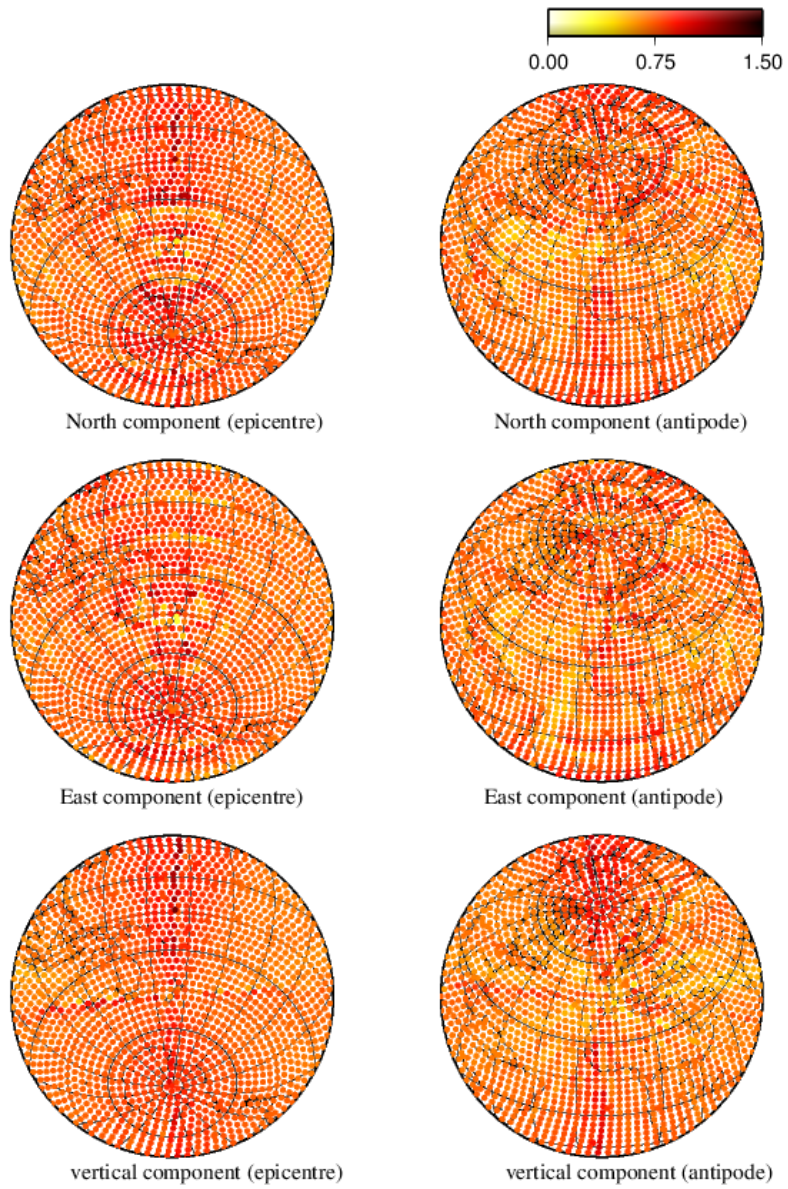


Figure 15: The waveform misfit between the centroid and two smaller sources of equal size, placed 50km apart. This data has been filtered to the SURF window.

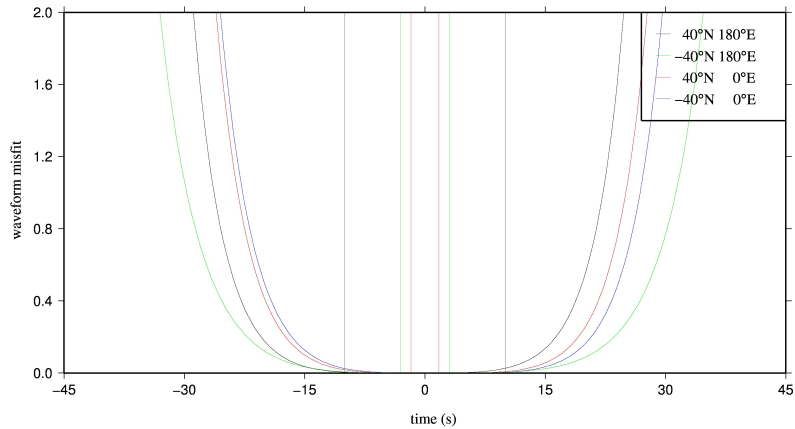


Figure 16: The waveform misfit of the East component between the centroid located at 12 km depth and two smaller sources, placed approximately 10 km apart, versus the temporal offset between the smaller sources. This data has been filtered to the SURF window. The vertical red, green and blue lines represent the time offset resulting from rupture speeds of 5700m/s, 3300m/s and 1000m/s respectively.

3.4 Splitting the source in space and time

Combining offset in time and space for the event located at 12 kilometres depth, we can observe a clear directional dependence on offset for the misfit function for larger offset (figures 16, 17 and 18). At approximately 10 km offset this directional dependence is not very large, but it is visible that the way the misfit changes with offset for different stations depends on the order in which the sources go off. This becomes even more clear for sources at 20 km apart, where the misfit differs substantially for each station depending on which source has gone off first. The misfit for an offset of 50 km does not even approach 0 and every station has a minimum in the misfit for significantly different offsets in time. This is likely due to constructive and destructive interference of the seismic wave-fields. If the seismic waveforms add up destructively, the size of the data decreases and the least squares misfit becomes larger for a similar difference compared to when there is constructive interference. This directional effect in the misfit is visible across the globe in figures 19, 20 and 21.

Of course, different parts of a seismic event will not go off at random intervals, but will most likely be triggered by each other. The time difference between segments going off will often depend on the rupture speed. The fastest possible rupture speed is equal to the P-wave velocity, but speeds closer to the S-wave velocity, if not slower, are also reasonable. The vertical lines in figures 16, 17 and 18 represent different rupture speeds, namely reasonable P- and S-velocities for in the crust as well as a lower end rupturespeed of 1km/s. For the smaller events, the range of wavespeeds encompasses an area of mostly negligible misfit, although for 20 km, slower subshear-velocity rupture times can give a very significant misfit already. This indicates that if the segments trigger each other with rupturespeeds that are not too slow, then the point source approximation will be accurate. This is not the case for an offset of 50 kilometres. It is possible that a different fault segment is not triggered directly by the first segment, but rather by a sequence of segments rupturing around it, this way the duration of the offset between the first and last segment could become larger than would be expected from the rupture speed, possibly leading to a greater misfit with the centroid.

3.5 A more realistic moment tensor distribution from InSAR data

So far we have looked at a source split into two parts. In reality a seismic source will often consist of more than two parts. Like the earthquake that hit Darfield New Zealand at 16:35 on 3 September 2010

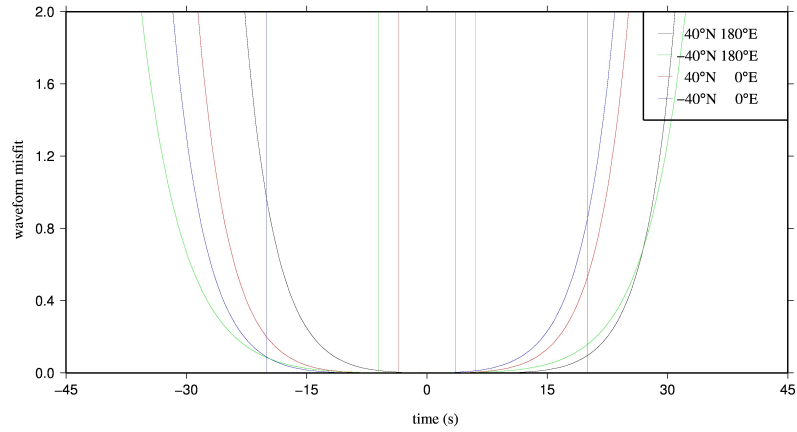


Figure 17: The waveform misfit of the East component between the centroid located at 12 km depth and two smaller sources, placed approximately 20 km apart, versus the temporal offset between the smaller sources. This data has been filtered to the SURF window. The vertical red, green and blue lines represent the time offset resulting from rupturespeeds of 5700m/s, 3300m/s and 1000m/s respectively.

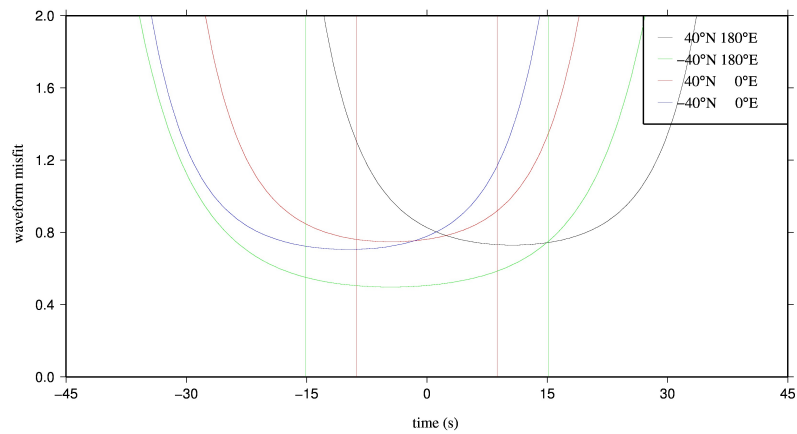


Figure 18: The waveform misfit of the East component between the centroid located at 12 km depth and two smaller sources, placed approximately 50 km apart, versus the temporal offset between the smaller sources. This data has been filtered to the SURF window. The vertical red and green lines represent the time offset resulting from rupturespeeds of 5700m/s and 3300m/s respectively.

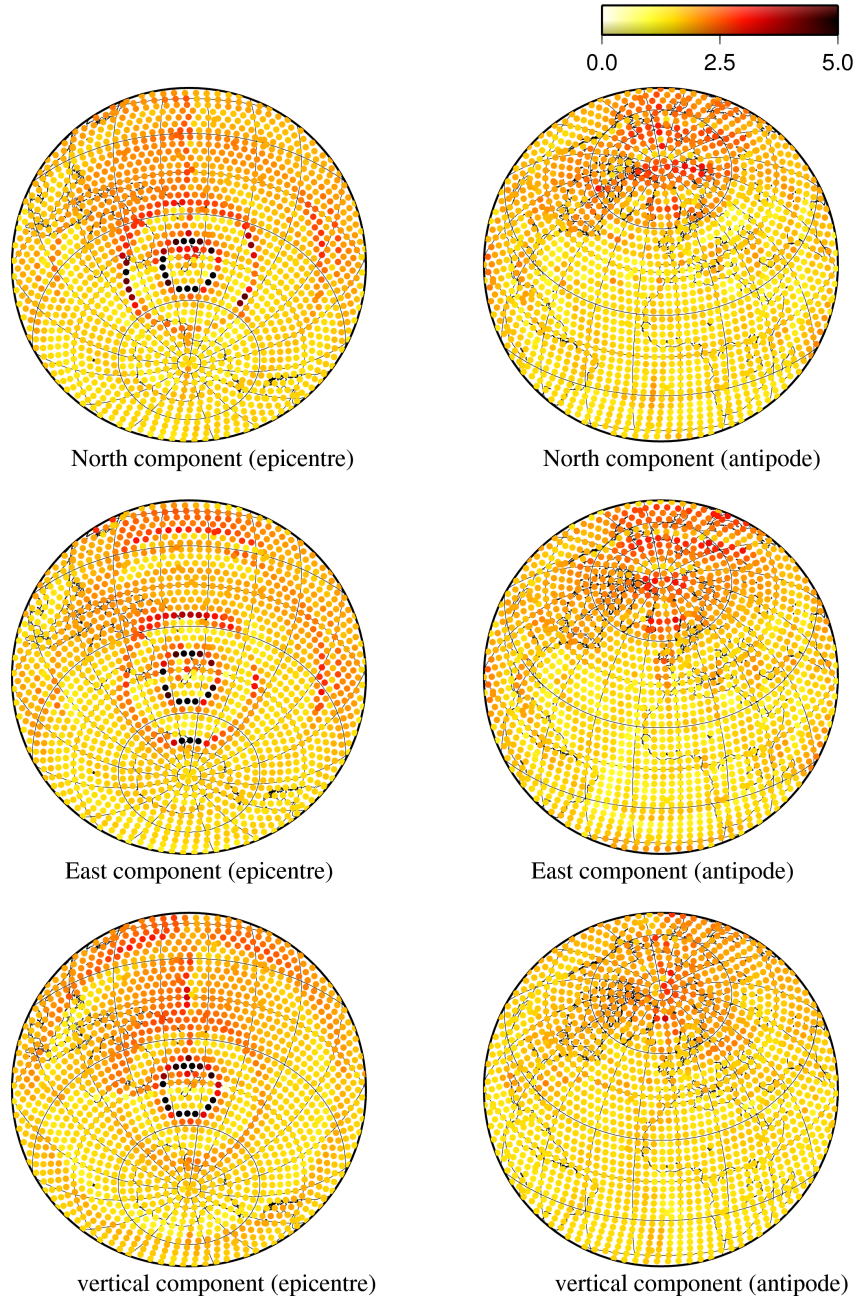


Figure 19: The waveform misfit between the centroid, located at approximately 12 km depth, and two smaller sources of equal size, placed 50km and 20 seconds apart. This data has been filtered to the BODY window.

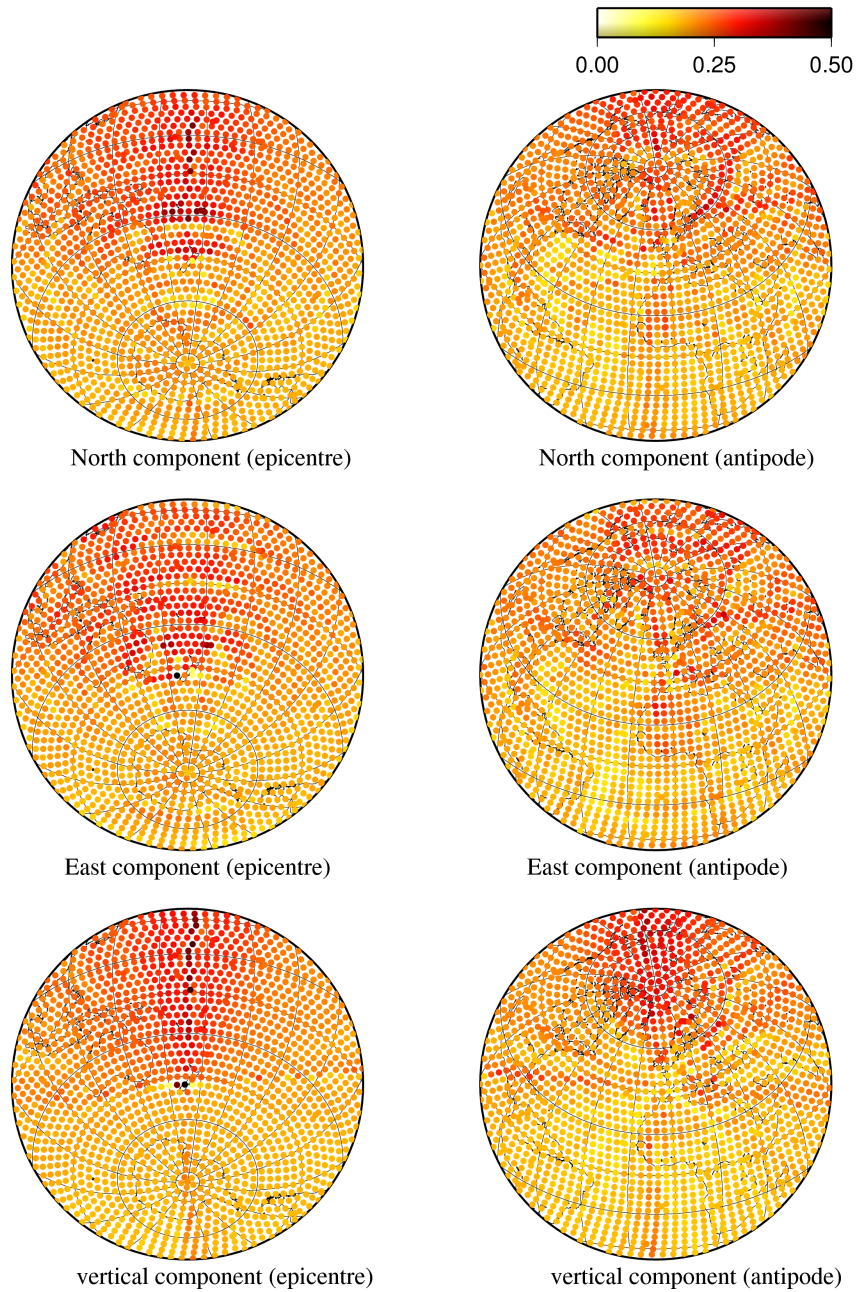


Figure 20: The waveform misfit between the centroid, located at approximately 12 km depth, and two smaller sources of equal size, placed 20km and 10 seconds apart. This data has been filtered to the SURF window.

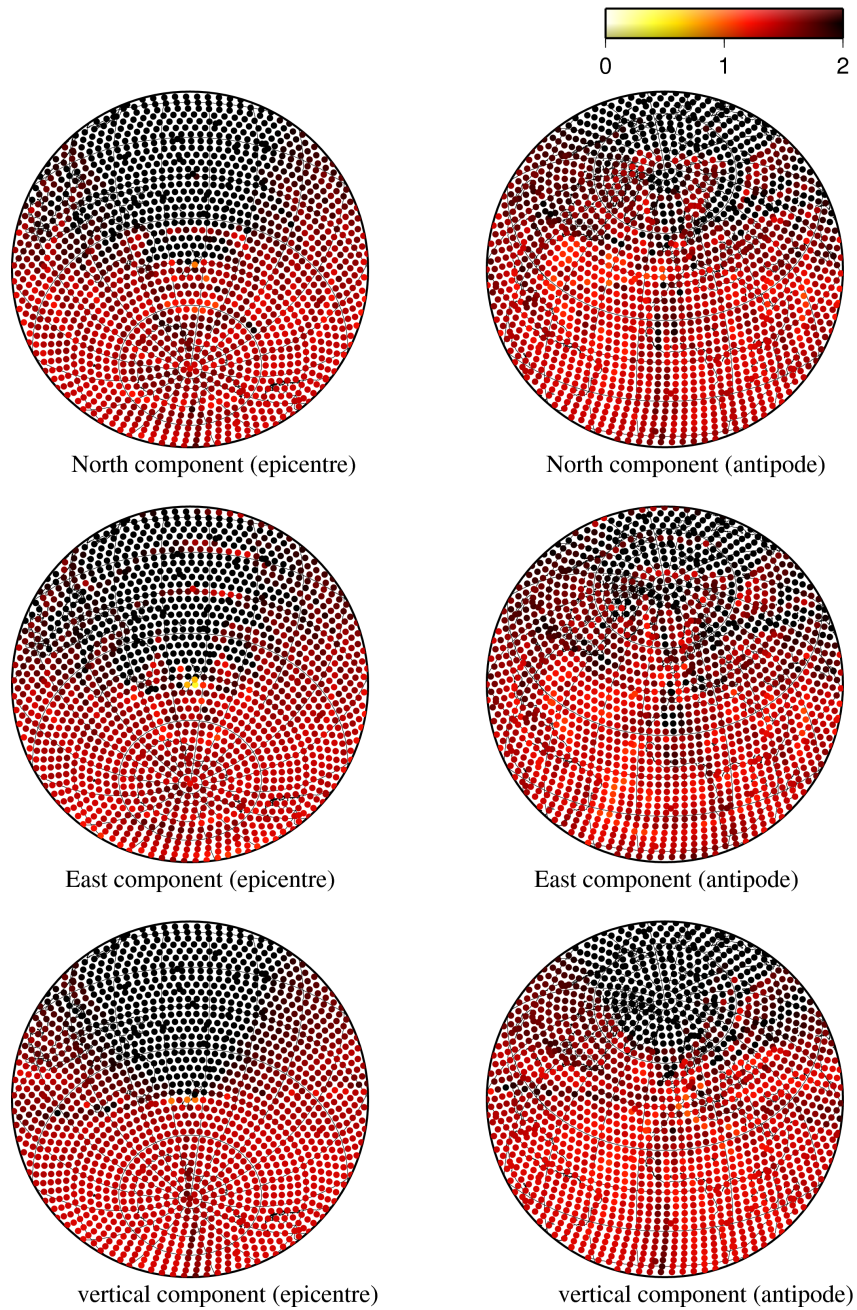


Figure 21: The waveform misfit between the centroid, located at approximately 12 km depth, and two smaller sources of equal size, placed 50km and 10 seconds apart. This data has been filtered to the SURF window.

(UTC). This earthquake has been studied using InSAR by Elliot et al. (2012). They identify a total of 8 fault segments as given in table 2. Although these segments would probably not have ruptured at the same time and for the same duration, we will assume this is the case. We calculate the centroid moment tensor for this distribution and, again, compare the seismograms generated for both cases. Figures 22 and 23 shows the results. For most of the stations the misfit is extremely small, but various shapes of significantly larger misfit than the surrounding stations are visible. The misfit for the stations located in these shapes is still not very large compared with the data but it does show that for more complicated distributions of the seismic moment, areas may arise where there is a comparatively large misfit, even far from the source.

4 Discussion

In this study we have investigated several simple cases with a very small number of distributed point sources, while a real distribution would be more continuous. Even though this is the case, we can still use these examples to say something about the combining of a distribution of point source moment tensors into a centroid moment tensor. It is also important to keep in mind that an event consisting of two point sources at a certain distance from each other, will represent an event with larger dimensions since it is unlikely that all of the seismic moment is released at the very edges of any event. Keeping this in mind, the fact that the least squares misfit for two sources placed apart in space versus the corresponding centroid is very small for distances of 20 kilometres and smaller and is quite significant for a distance of 50 kilometres does not necessarily indicate that the maximum size of an event must be smaller than 50 km, although it will probably not be much larger. Such lengths are considerably smaller than the wavelength of the waves used in the time-frequency windows, which should be several hundreds of kilometres for most of the frequency range. Of course, it is possible that smoother distributions of point sources may allow for larger areas. The wavelength of the waves used here should be upwards of 150 kilometres, over three times the length of the largest offset investigated here, although that offsets used here would probably represent faults of greater length because it is unlikely that all energy is released at the very ends of a fault.

If we look at a more realistic distribution of sources as for the Darfield earthquake, we can see that patterns of higher misfit develop. While the misfit in this case is still very small, it is still important to note that in reality seismic station coverage is much more limited and if the majority of stations happen to fall in regions of higher misfit, then that could translate into any inversions. Even a few highly anomalous stations could introduce significant bias in the results. In this particular case the majority of the stations from the IRIS/IDA and IRIS/USGS networks do not fall in this region, although several stations do fall in areas with comparatively high misfit.

If we look at sources split up in time, we may be able to say something about the duration of an event for which a single centroid time could be representative. Splitting the moment tensor in two and simply triggering the sources at different times may not be entirely realistic but it could represent a fault slipping in very short bursts, or different segments triggering at different times. Overall, if the sources trigger within 15 seconds, the misfit remains quite small and in the case of a difference of 7 seconds, the misfit is negligible.

In the case where source time functions are implemented, we have a sense of the duration of an event. If each source has a triangular source time function with a half-width of 7.5 seconds and is offset by 20 seconds, the total duration of the event will be 35 seconds. This seems close to the maximum duration that can be approximated by a centroid moment tensor with a triangular source time function with the same half-width as the smaller sources, within the time-frequency windows used here. More accurate source time functions seem to be able to help increase this, which would mean that durations close to the lower end periods of the time-frequency windows can still be quite accurately represented by a centroid moment tensor. The misfit, however appears to be dominated by the distance between the peaks of activity for both point sources rather than the duration. It also appears to be the case that, at least for these experiments, splitting a point source into multiple smaller point sources does not give the same result at longer wavelengths, as distributing energy release through source-time functions.

Combining splitting in space and time does show some directional effects as well as increases in the least squares misfit compared to offsets in time or space only. This means that more realistic seismic sources that can be accurately represented by a centroid moment tensor will be limited to

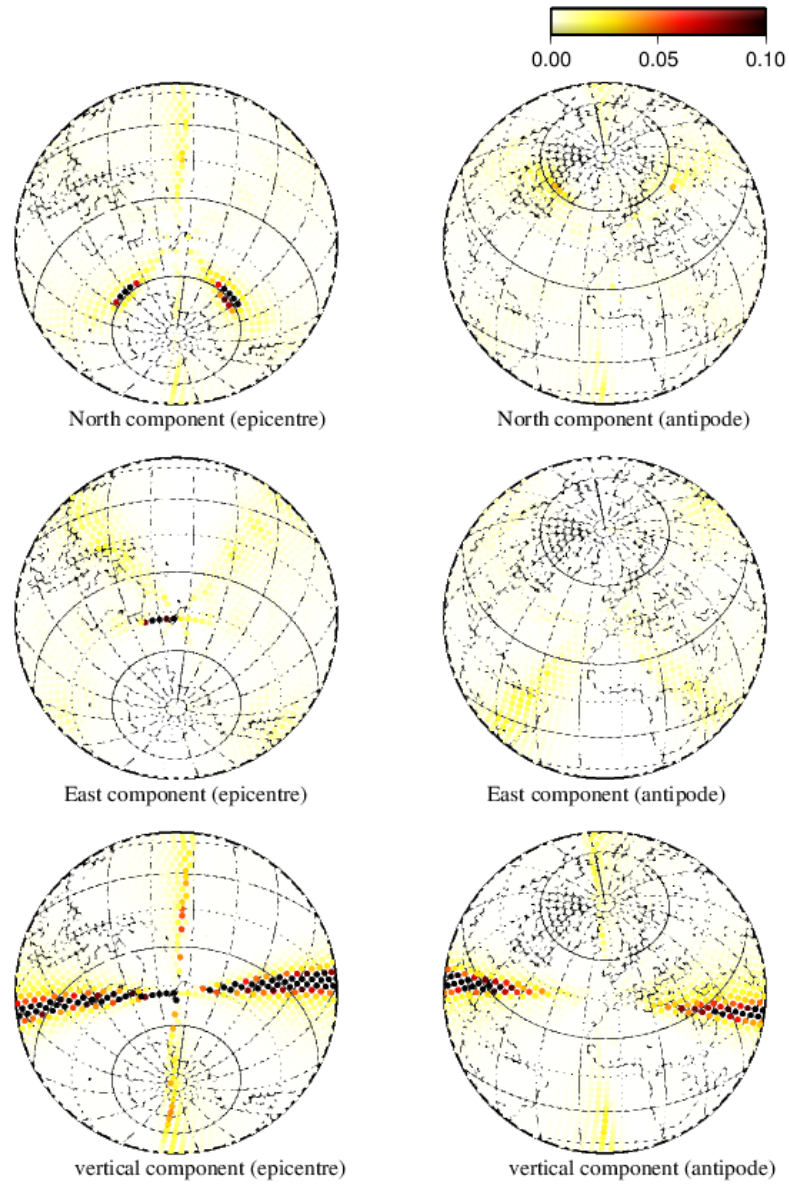


Figure 22: The waveform misfit between the distribution of moment tensors for the Darfield earthquake as determined by Elliot et al. (2012) versus the corresponding centroid moment tensor. This data has been filtered to the SURF window.

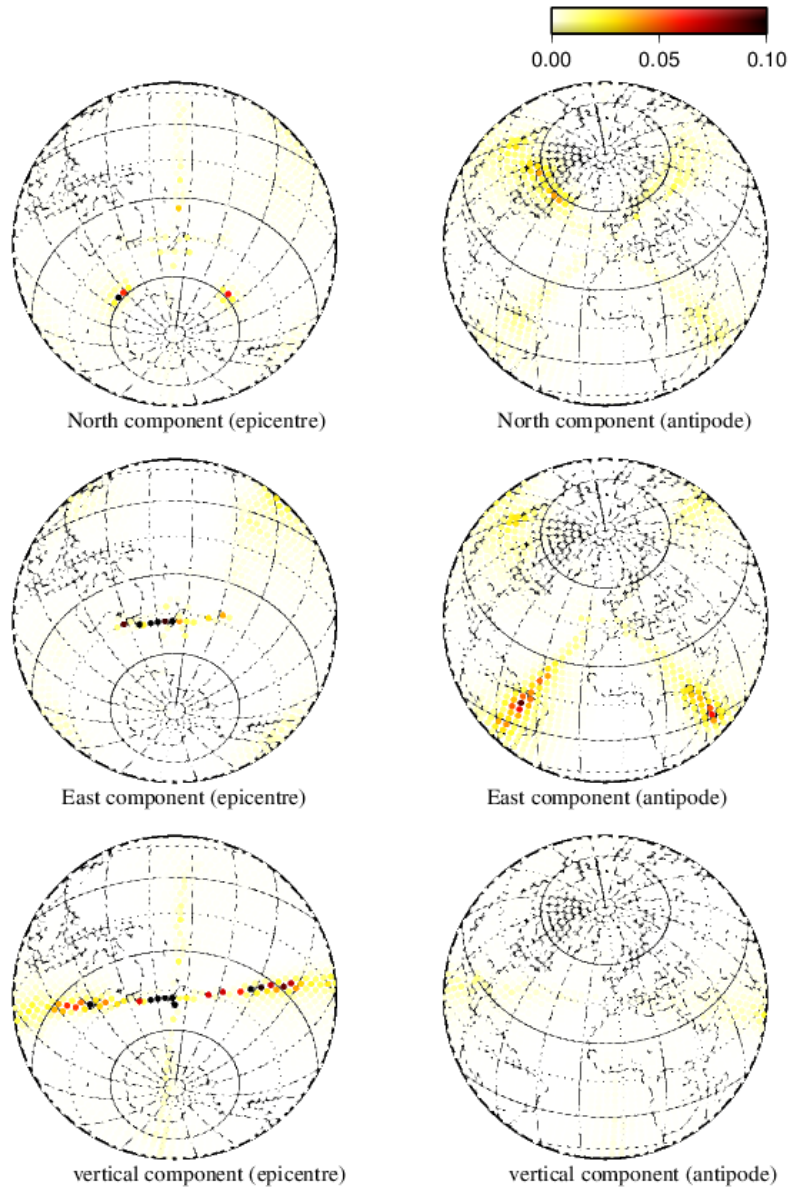


Figure 23: The waveform misfit between the distribution of moment tensors for the Darfield earthquake as determined by Elliot et al. (2012) versus the corresponding centroid moment tensor. This data has been filtered to the BODY window.

shorter durations and/or smaller spatial dimensions. Realistic rupture speeds appear to indicate that the duration of an event will often be short enough for this not to be a problem, as long as the spatial dimensions of the event are not too large.

We are using the crust2.0 model, which has lateral variations in material properties. This means that the same point source, located at different positions may be characterized by the different properties of the environment, affecting the energy release and the generated wave-field, even though it is described by the same moment tensor. This is an additional effect that can affect the misfit in our experiments. It is especially important for larger distances between sources, where the individual sources may occur in different environments to each other as well as to the centroid. If this has an impact in our experiments, then that also carries over to reality, where different parts of an event will be characterized by a different rupturing environment, even more so than in the crust2.0 model, meaning that, for sources with large spatial dimensions, there will always be a misfit introduced by this fact.

5 Conclusions

The statement that a distribution of point sources can be accurately represented by a single centroid moment tensor as long as the periods of the waves investigated are significantly longer than the duration of the source and the wavelength is considerably larger than the dimensions of the event appears to hold out pretty well, as long as the spatial dimensions of the event do not become too large. According to the few experiments performed in this study, acceptable durations approach the lower end of the periods used. However, the misfit in the experiments appears to be dominated by the time between peak activity of the two sources, rather than the total duration. Also, more exact source-time functions increase the misfit for shorter intervals between peak activity. For spatial offsets approaching one third of the lower end of the wavelengths, the misfit becomes very significant. Realistic rupture speeds show that the misfit for smaller events should not be very large. Larger events show considerable misfit and when looking at the Darfield event, consisting of multiple segments, there is a very uneven distribution of misfit. This could lead to considerable bias, depending on the location of seismic stations used in a study.

This study only looked at a handful of examples and more investigation is needed before any definitive conclusions can be drawn. It is, however, important for researchers using the point source approximation, to be aware of the fact that even for longer period data, there may be significant differences between the seismic signal of an event and that of the corresponding point source. Sources with large spatial dimensions or those consisting of multiple segments should be treated with extra care because of this.

References

- Backus, G. E. (1977). Interpreting the seismic glut moments of total degree two or less. *Geophysical Journal of the Royal Astronomical Society*, 51:1–25.
- Backus, G. E. and Mulcahy, M. (1976). Moment tensors and other phenomenological descriptions of seismic sources—i. continuous displacements. *Geophysical Journal of the Royal Astronomical Society*, 46:341–361.
- Bassin, C., Laske, G., and Masters, G. (2000). The current limits of resolution for surface wave tomography in north america. *Eos*, 81.
- Dziewonski, A., Chou, T.-A., and Woodhouse, J. (1981). Determination of earthquake source parameters from waveform data for studies of global and regional seismicity. *Journal of Geophysical Research*, 86:2825–2852.
- Dziewonski, A. and Woodhouse, J. (1983). Studies of the seismic source using normal-mode theory. In Kanamori, H. and Boschi, E., editors, *Earthquakes: observation, theory, and interpretation*, Proceedings of the International School of Physics “Enrico Fermi”, pages 45–137. North-Holland, Amsterdam.
- Ekström, G., Nettles, M., and Dziewoński, A. M. (2012). The global cmt project 2004-2010: Centroid-moment tensors for 13,017 earthquakes. *Physics of the Earth and Planetary Interiors*, 200–201:1–9.

- Elliot, J. R., Nissen, E. K., England, P. C., Jackson, J., Lamb, S., Li, Z., Oehlers, M., and Parsons, B. (2012). Slip in the 2010–2011 canterbury earthquakes, new zealand. *Journal of Geophysical Research*, 117(B03401).
- Komatitsch, D., Erlebacher, G., Göddeke, D., and Michéa, D. (2010). High-order finite-element seismic wave propagation modeling with mpi on a large cpu cluster. *Journal of Computational Physics*, 229:7692–7714.
- Komatitsch, D. and Tromp, J. (2002a). Spectral-element simulations of global seismic wave propagation i: validation. *Geophysical Journal International*, 149:390–412.
- Komatitsch, D. and Tromp, J. (2002b). Spectral-element simulations of global seismic wave propagation ii: Three-dimensional models, oceans, rotation and self-gravitation. *Geophysical Journal International*, 150:303–318.
- Madariaga, R. (2007). Seismic source theory. In Schubert, G., editor, *Treatise on Geophysics*, volume 4, chapter 4.02, pages 59–82. Elsevier, Amsterdam.
- Panning, M. and Romanowicz, B. (2006). A three-dimensional radially anisotropic model of shear velocity in the whole mantle. *Geophysical Journal International*, 167:361–379.
- Ritsema, J., Deuss, A., van Heijst, H.J., and Woodhouse, J. (2011). S40rts: a degree-40 shear-velocity model for the mantle from new rayleigh wave dispersion, teleseismic traveltime and normal-mode splitting function measurements. *Geophysical Journal International*, 184:1223–1236.
- Ritsema, J., van Heijst, H. J., and Woodhouse, J. H. (1999). Complex shear wave velocity structure imaged beneath africa and iceland. *Science*, 286:1925–1928.
- Valentine, A. and Trampert, J. (2012). Assessing the uncertainties on seismic source parameters: Towards realistic error estimates for centroid-moment-tensor determinations. *Physics of the Earth and Planetary Interiors*, 210-211:36–49.